Applied Physics Letters

RESEARCH ARTICLE | JULY 24 2023

Coexistence of infrared plasmon and thermoelectricity in rare-earth semiconducting ytterbium nitride FREE

Mehak Loyal ; Bidesh Biswas ; Prasanna Das ; Bivas Saha

Appl. Phys. Lett. 123, 042101 (2023)
https://doi.org/10.1063/5.0160396

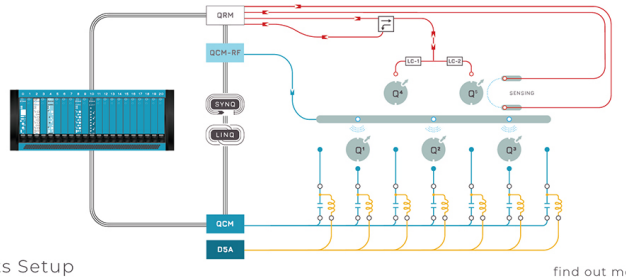

AIP Publishing

Applied Physics Letters ARTICLE pubs.aip.org/aip/apl

Coexistence of infrared plasmon and thermoelectricity in rare-earth semiconducting ytterbium nitride

Cite as: Appl. Phys. Lett. **123**, 042101 (2023); doi: 10.1063/5.0160396
Submitted: 1 June 2023 · Accepted: 11 July 2023 ·
Published Online: 24 July 2023

Mehak Loyal,[1,2] Bidesh Biswas,[1,2] Prasanna Das,[1,2] and Bivas Saha[1,2,3,a)]

AFFILIATIONS

[1]Chemistry and Physics of Materials Unit, Jawaharlal Nehru Centre for Advanced Scientific Research, Bangalore 560064, India
[2]International Centre for Materials Science, Jawaharlal Nehru Centre for Advanced Scientific Research, Bangalore 560064, India
[3]School of Advanced Materials (SAMat), Jawaharlal Nehru Centre for Advanced Scientific Research, Bangalore 560064, India

[a)]Author to whom correspondence should be addressed: bsaha@jncasr.ac.in and bivas.mat@gmail.com

ABSTRACT

Rare-earth nitride (REN) pnictides are exciting materials due to their localized and strongly correlated 4*f*-electrons that lead to interesting magnetic properties useful for spintronic devices. Ytterbium nitride (YbN) is a unique rare-earth pnictide as it exhibits antiferromagnetic ground states, unlike most ferromagnetic RENs. Though the magnetic properties of YbN thin films have been studied before, the electronic, thermoelectric, and plasmonic properties of YbN are yet to be investigated. Here, we show coexisting high thermoelectric power factor and short-wavelength infrared plasmon polaritons in epitaxial YbN thin films deposited with the ultrahigh vacuum growth method. YbN thin films deposited on (001) MgO substrates exhibit epitaxial and good quality crystalline growth and exhibit a high thermoelectric power factor of $\sim$ 1.9 mW/mK^2 at 750 K due to high electrical conductivity and a moderately high Seebeck coefficient. High carrier concentration also leads to a positive-to-negative dielectric permittivity transition in YbN at $\sim$1900–1950 nm, corresponding to the epsilon-near-zero plasmonic resonance. Low-temperature transport measurements revealed that dislocation and acoustic phonon scattering dominate electronic transport. Demonstration of coexisting high thermoelectric power factor and infrared plasmon polaritons marks important progress in designing YbN-based thermoelectric and plasmonic devices for future applications.

Rare-earth semiconducting nitrides are an emerging class of materials with distinct electronic and magnetic properties. RENs are currently explored experimentally for various applications, including spintronics, infrared (IR) detectors, cryo-coolers, scintillators for high-energy particle detection, and contacts for III–V compound semiconductors.[1–6] Localized and strongly correlated 4*f*-electrons in RENs generally lead to ferromagnetic ground states that are attractive for spintronic devices and spin-superlattices.[7–10] Similarly, rare-earth-doped semiconductors are also explored for their dilute magnetic semiconducting properties and exotic spin-textures.[11–13] Solid-state alloys of RENs with III–V compound semiconductors have been used to develop solid-state lasers, amplifiers, and light-emitting devices in the infrared spectral range for the retina-safe and fiber optical communication wavelength ranges.[14,15] With intra-*f* or *d*-*f* electronic transition, RENs are also used in wide bandgap semiconductors for scintillators in high-energy particle detections, especially for neutrons.[1,16] Recently, some RENs have also exhibited high thermoelectric power factor and potential for high figure-of-merit (zT) at high temperatures that could be useful for their energy conversion device applications.[17]

Ytterbium nitride (YbN) is the second-heaviest REN and has found applications as additives for special alloys and non-ferrous metals, as a phosphor, and as ceramic materials.[18,19] In one of the earliest reports in 1963, YbN bulk crystals were synthesized by nitriding Yb metals by prolonged heat treatment with an ammonia environment.[20] YbN obtained with this method contained some amount of Yb^{2+} divalent ions and exhibited semiconducting behavior with high *n*-type carrier concentration and low mobility. Importantly, magnetic measurements showed an antiferromagnetic ground state in YbN, which is markedly different from the ferromagnetism exhibited by most other RENs. Subsequent specific heat measurements on bulk YbN crystals showed cooperative phase transitions below 1 K and suggested a high density of electronic states at the Fermi level, prompting the authors to conclude that YbN is a heavy-fermion.[21] However, further optical

reflection experiments on stoichiometric and off-stoichiometric YbN found the highest occupied $4f^{13}$ bands at ~6 eV below the Fermi level and the lowest unoccupied $4f^{14}$ band at ~0.2 eV above the Fermi level, and an effective mass of the carriers to be 2.2 m_0.[22] Such moderate carrier effective mass, *p-f* hybridization, and a small amount of *f-d* hybridization led to the conclusion that YbN is unlikely to be a heavy fermion and more likely to be a Kondo insulator.

Compared to the bulk crystals, thin films of YbN are seldom studied. In one of the only experimental reports, polycrystalline YbN thin films are deposited by evaporating Yb metal under an activated nitrogen partial pressure using an ion source.[23] GaN is further deposited as capping layers to protect the surface from oxidation. YbN films obtained with this method exhibited an antiferromagnetic ground state with a Neel temperature of 93 ± 3 K and $\mu_{\text{eff}} = (4.5 \pm 0.1)\ \mu B$ per Yb ion. Low-temperature electrical measurements also showed a negative temperature coefficient of resistance and high carrier concentration that is consistent with its degenerate semiconducting nature. Theoretically, local spin density approximation (LSDA) along with Hubbard U corrections is used to model the electronic and magnetic structure of YbN.[24] Results showed that depending on the initial structure and spin alignments, the theoretical ground state converges into either trivalent (Yb^{3+}) or divalent (Yb^{2+}) oxidation states. The electronic structure of YbN also strongly depends on the valency of the Yb cation. The filled *4f* states lie lower inside the valence band in Yb^{3+}, and the unoccupied *4f* bands strongly hybridize with the N-*2p* bands. However, the filled *4f* states are much closer to the Fermi energy for divalent cases. A direct X–X gap of 1.35 eV and an indirect Γ–X gap of 0.68 eV are predicted from these theoretical calculations.[24,25]

Though the previous experimental and theoretical research on YbN has been noteworthy, for practical device applications, it is necessary to characterize the electronic, optical, thermoelectric, and plasmonic properties in greater detail, preferably in single-crystalline thin films. Therefore, with the motivation of developing YbN-based electronic, thermoelectric, and plasmonic devices, and with the prospect of its epitaxial integration with other III-nitride semiconductors, in this work, we present epitaxial and good quality YbN thin films deposited with ultra-high vacuum (UHV) growth methods. Transparent AlN thin film coatings are deposited *in situ* on YbN as capping layers to prevent oxidation. YbN thin films exhibit a high thermoelectric power factor on par with the best-known thermoelectric materials, such as Bi_2Te_3[26] and Zn_4Sb_3.[27] In addition, they also show a short-wavelength infrared plasmonic response that makes it attractive for detectors, sensors, and telecommunication applications.[1,14,15]

YbN thin films of thickness 125 nm are deposited on (001) MgO (YbN/MgO) and (0001) Al_2O_3 (YbN/Al_2O_3) substrates with a dc-magnetron sputtering inside a UHV chamber with a base pressure of 1×10^{-9} Torr at 900 °C. Details on the growth and characterization methods are presented in the supplementary material (SM) section. Without a capping layer, as-deposited YbN thin films have a brownish-red tint [see Fig. S1(a)] and oxidize in ambient air within 15–20 min of being removed from the UHV chamber. YbN film's brownish-red hue is close to that of ErN[17] and ScN,[28,29] demonstrating their comparable optical properties. After oxidation, the color of the film changes to light green [see Fig. S1(b)]. Therefore, a thin layer of AlN was deposited *in situ* on top of YbN while maintaining the same deposition temperature to stabilize YbN in ambient conditions. The resulting YbN was observed to be ambient stable for at least 5 months [see Fig. S1(d)] despite having a somewhat darker appearance. AlN is well recognized for its oxidation resistance due to the formation of a thin Al_2O_3 coating on its surface, which serves as an oxidation protective barrier. To measure the electrical and thermoelectric properties,[17] AlN layer thickness was restricted to ~2–3 nm. For structural characterization and optical property analysis, the capping layer thickness was increased to 20 nm.

Symmetric 2θ-ω high-resolution x-ray diffraction (HRXRD) measurements on YbN deposited on the (001) MgO substrate show that the film exhibits a single (111) orientation [see Fig. 1(a)]. While other rock salt semiconductors, such as ScN[28,29] and CrN,[35] exhibit smaller lattice-mismatch and grow with (002) orientations on (001) MgO substrates, YbN grows with (111) orientation on the (001) MgO substrate due to the large lattice-mismatch of ~15%. The (111) YbN film 2θ-peak on (001) MgO appears at 32.2°, which results in a *c*-plane lattice constant of 4.81 Å. This *c*-axis lattice constant is close to its bulk lattice parameter.[20] The full-width-at-the-half-maxima (FWHM) of the rocking curve corresponding to the (111) plane of YbN is 0.43°, which suggests its good crystalline quality. The pole figure measurement of YbN/MgO for (220) reflection shows 24 symmetrically positioned diffraction spots of similar intensity [see Fig. 1(b)]. These diffraction spots are the rotational twin planes of {220} around [111] direction. These 24 diffraction spots form equidistant 12 pairs, symmetrically placed 30° apart from each other, indicating twisting (~10°) among twin domains. The extensive twinning could be explained by a significant lattice mismatch between YbN and MgO of

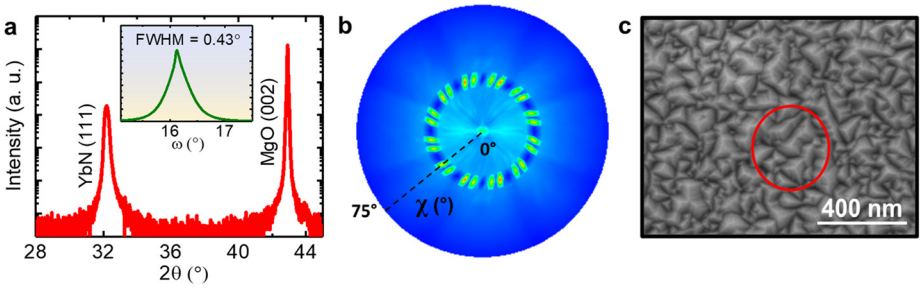

FIG. 1. (a) Symmetric 2θ-ω HRXRD pattern for YbN deposited on MgO (001) substrates. The film grows with only one (111) orientation. Inset in the figure shows that the FWHM of ω-scan (rocking curve) is 0.43° that highlights its good crystalline property. (b) Pole-figure of YbN corresponding to (220) reflection is presented showing twisted domains, and (c) plan-view SEM images of YbN/MgO showing triangular (111) oriented growth; the red circle highlights the twinning of domains.

15%. The x-ray profile intensities are elliptic, with orientation changes along the rotation angle around the surface normal, indicating the tilt-induced broadening of the reciprocal lattice points. The plan-view FESEM image of the film deposited on the (001) MgO substrate [Fig. 1(c)] show merged triangular grains showing the (111) orientation. Twinning can be seen in the image. Unlike YbN films deposited on the (001) MgO substrate, YbN deposited on the (0001) Al_2O_3 substrate exhibits textured growth with two different orientations, namely, (200) and (111) [see Fig. S2(a)].

X-ray photoelectron spectroscopy (XPS) measurement is performed to analyze the chemical states of Yb and N using a monochromatic Al-K_α x-ray source (see Fig. 2). Before the measurement, the 2-nm-thick AlN capping layer is removed using 1 keV Ar^+ ion sputter etching. High-resolution Yb-*4d*, Yb-*4p*, N-*1s*, and O-*1s* peaks are calibrated using the C-*1s* photoelectron signal at 284.6 eV as a reference. The Yb *4d* XPS spectrum is found to be complicated and is quite similar to the spectrum reported for several other Yb-based compounds.[30–32] It can be deconvoluted into seven peaks due to LS coupling that divides the final state of $4d^9$ and $4f^{13}$ into the ^{3}(HGFDP) and ^{1}(HGFDP) state.[30] The peaks at 183.2 and 190.7 eV are assigned to the $4d_{5/2}$ and $4d_{3/2}$ components of Yb^{3+}, and the corresponding shoulders at 180.3 and 187.2 eV are assigned to $4d_{5/2}$ and $4d_{3/2}$ components of Yb^{2+}. With a probability of 0.031, Yb^{2+} ions are less prevalent than Yb^{3+} ions. The presence of Yb^{2+} causes a slightly higher lattice constant (4.81 Å) compared to bulk values (4.78 Å) as the ionic radius of Yb^{2+} is greater than the Yb^{3+} ion. The Yb *4p* spectrum also shows the mixed valence states. Peaks at 344.3 and 394.8 eV are assigned to Yb $4p_{3/2}$ and Yb $4p_{1/2}$, respectively. There is a large spin–orbit splitting of 50.5 eV due to the significant effect of LS coupling. The N-*1s* spectra coincide with the Yb $4p_{1/2}$. The N-*1s* deconvoluted peaks at 395.2 and 397.6 eV are attributed to the presence of N in N–Yb and N–Yb–O bonds, respectively. For O-*1s*, two peaks were observed at binding energies of 530.9 and 529 eV, which correspond to the O–N–Yb and O–Yb bonds, respectively. Despite the protective layer, oxygen impurity is present as Yb_2O_3 in the film due to the high affinity of Yb toward oxygen. The optical absorption measurements are performed to determine the bandgap of YbN films. Results show (see supplementary material section 4) that YbN/MgO and YbN/Al_2O_3 exhibit a direct optical bandgap of 1.78 and 1.86 eV, respectively. These bandgap values are consistent with previous literature reports.[23–25]

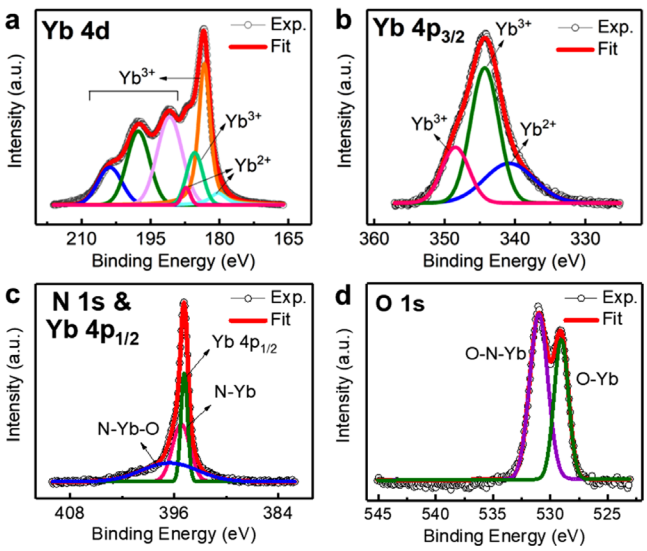

FIG. 2. High-resolution XPS core-level spectra of a YbN thin film corresponding to (a) Yb-*4d*, (b) Yb-$4p_{3/2}$, (c) N-*1s* & Yb-$4p_{1/2}$, and (d) O *1s*. They are deconvoluted into Gaussian peaks. The Yb *4d* and $4p_{3/2}$ spectra are strongly affected by LS coupling and show the presence of mixed valence states (Yb^{2+} and Yb^{3+}) with a primarily trivalent component.

Room-temperature Hall measurements (see Table I) show that YbN films deposited on (001) MgO exhibit a high electron mobility of 23.1 cm^2/V s, significantly higher than the mobilities previously reported[20,23] in YbN bulk crystals and thin films. Such high mobility is about eight times larger than the highest mobility reported[33] for ErN thin films deposited on (001) MgO substrates with similar growth conditions. Hall measurements also show YbN/MgO exhibiting a large *n*-type carrier concentration of 1.4×10^{21} cm^{-3}, presumably due to nitrogen vacancies and oxygen impurity.[36,37] Such high mobility and carrier concentration leads to a room-temperature resistivity of 1.9×10^{-4} Ω cm in YbN/MgO, showing its degenerate semiconducting nature. Though the room-temperature resistivity of YbN compares well with the resistivity of well-known rock salt III(B) scandium nitride (ScN),[28,29] the carrier mobility is relatively smaller in YbN. Therefore, with subsequent changes in growth conditions, it should be possible to increase mobility further. Compared to the YbN/MgO, YbN/Al_2O_3 exhibits much lower mobility and lower carrier concentration. The higher mobility of YbN/MgO can be directly attributed to the better crystalline quality of the YbN/MgO films. YbN deposited on (001) MgO substrates exhibits epitaxial growth with a single (111) orientation with a small 0.43 ° FWHM of the rocking curve. On the contrary, the YbN/Al_2O_3 films are textured and show two different growth orientations (111) and (001). Therefore, better crystalline quality leads to higher mobility in YbN/MgO. The slightly larger carrier concentration of YbN/MgO compared to the YbN/Al_2O_3 could be associated with the presence of a slightly higher concentration of electronically active defects, such as oxygen impurity or nitrogen vacancies.

To gain further insight into the carrier scattering mechanism, temperature-dependent Hall measurement is performed from the 50 to 400 K range for YbN/MgO (see Fig. 3). Results show that the mobility decreases with an increase in temperature. The experimental temperature-dependent mobility is theoretically fitted considering contributions from ionized impurity ($\mu_{\text{ionized impurity}}$) and dislocation scattering ($\mu_{\text{dislocation}}$) to elucidate the scattering processes, using the following equations:

$$\mu_{\text{ionized impurity}} = AT^{1.5}, \tag{1}$$

where A = constant and T = absolute temperature, and

TABLE I. Room temperature Hall measurement result for YbN on the MgO and Al_2O_3 substrates.

Electronic properties	YbN/MgO	YbN/Al_2O_3
Carrier concentration (/cm^3)	1.4×10^{21}	8.7×10^{20}
Mobility (cm^2/V s)	23.1	3.0
Resistivity (Ω cm)	1.9×10^{-4}	2.33×10^{-3}

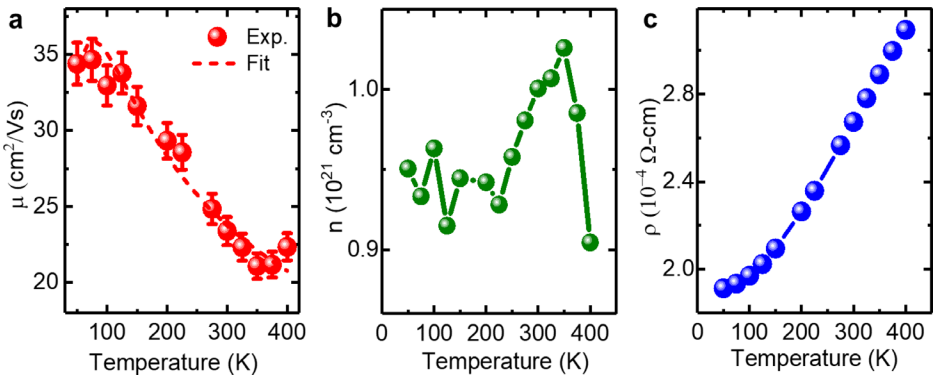

FIG. 3. Temperature-dependent (a) mobility, (b) carrier concentration, and (c) electrical resistivity of YbN thin film deposited on the (001) MgO substrate are presented. Due to its good crystallinity, YbN films exhibit a high electron mobility of 34.6 $cm^2/V\,s$ at 50 K. Mobility decreases with increasing temperature due to the dislocation and acoustic phonon scattering. The carrier concentration of YbN remains high and near constant with respect to temperature change. Resistivity increases with increasing temperature highlighting YbN's degenerate semiconducting nature.

$$\mu_{\text{dislocation}} = \left(\frac{3q}{8N_d R}\right)\frac{1}{(3m^* k_B T)^{0.5}}, \tag{2}$$

where q = electronic charge, N_d = dislocation density, R = dislocation core radius, m^* = effective mass, and k_B = Boltzmann constant.

The total mobility is calculated as

$$\frac{1}{\mu_{\text{total}}} = \frac{1}{\mu_{\text{ionized impurity}}} + \frac{1}{\mu_{\text{dislocation}}}. \tag{3}$$

The theoretical model [see Eqs. (1)–(3)] fits well with experimental results, revealing a dislocation density of $\sim 3.97 \times 10^{10}\ cm^{-2}$ and a dislocation core radius of ~4 nm. There is also a minor fluctuation in carrier concentration in the measured temperature (50–400 K) range. The increased electrical resistivity with the temperature rise corroborates that YbN is a degenerate semiconductor.

Seebeck coefficient (S) and electrical conductivity (σ) of YbN films are measured in the temperature range from 340 to 775 K [Figs. 4(a) and 4(b)] to analyze their potential for thermoelectric devices. At 340 K, YbN/MgO and YbN/Al_2O_3 exhibit a Seebeck coefficient of −52.2 and −72.7 μV/K, respectively. Seebeck coefficient increases monotonically and reaches −107.6 and −147.7 μV/K for the maximum temperature of 775 K for YbN/MgO and YbN/Al_2O_3, respectively. Such a high Seebeck coefficient of YbN is about five times larger than the values previously recorded in bulk samples.[20] Seebeck coefficient values in YbN are comparable to the ones measured for ScN[28,29] and are much higher than the Seebeck coefficient measured in ErN[17] thin films. The electrical conductivity decreases from 4.1×10^3 to $2.5 \times 10^3\ S\ cm^{-1}$ for YbN/MgO and from 0.361×10^3 to $0.306 \times 10^3\ S\ cm^{-1}$ for YbN/Al_2O_3 with the rise in temperature from 340 to 775 K, which follows the increase in the Seebeck coefficient. Consecutively, the thermoelectric power factor increases monotonically, reaching 1.93 $mW/m\,K^2$ for YbN/MgO and 0.68 $mW/m\,K^2$ for YbN/Al_2O_3 for the highest measured temperature of 775 K [see Fig. 4(c)]. The power factor of the YbN films deposited on a sapphire substrate is significantly lower than ScN[28,29] and compares well with ErN[17]. However, the power factor of YbN/MgO is higher than ErN[17] and comparable to ScN[28,29,34] and CrN[35] power factor. Therefore, these measurements show that YbN exhibits a large power factor comparable to the best-known thermoelectric materials, such as SnSe,[38] La_3Te_4,[39] and SiGe.[40]

With the large carrier concentration and high mobility, YbN thin films are expected to exhibit high-quality and low loss plasmonic responses. Therefore, the real and imaginary components of the dielectric permittivity of films are measured on both substrates with spectroscopic ellipsometry. Results show that the real component of the dielectric permittivity (ε') undergoes a positive-to-negative transition [epsilon-near-zero (ENZ)] at 1950 and 1900 nm for YbN/MgO and YbN/Al_2O_3, respectively. As ENZ wavelengths represent the onset of the metallic character, these results highlight YbN's short-wavelength infrared plasmonic properties. Consequent to the ENZ wavelength, $|\varepsilon'|$ increases monotonically at longer wavelengths due to its increasing metallicity. The magnitude of the imaginary part of the dielectric permittivity (ε'') representing optical loss at the crossover wavelength for YbN/MgO and YbN/Al_2O_3 is 2.64 and 2.40, respectively. These values suggest that the optical losses of YbN at the ENZ wavelength are slightly higher than the ones exhibited by ScN,[41] which has emerged as

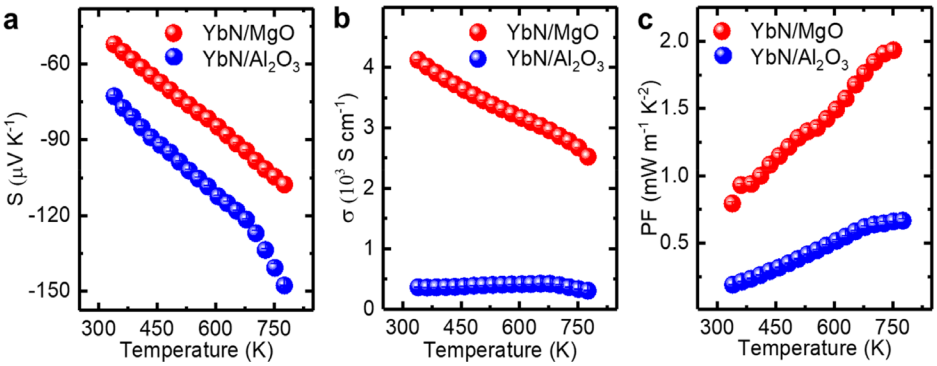

FIG. 4. (a) Seebeck coefficient, (b) electrical conductivity, and (c) thermoelectric power factor of YbN film deposited on the (001) MgO and (0001) Al_2O_3 substrates are presented. Seebeck coefficient increases with an increase in temperature and exhibits a maximum of −107.6 and −147.7 μV/K at 775 K for YbN/MgO and YbN/Al_2O_3. The power factor of YbN/MgO increases with a rise in temperature and exhibits a maximum of 1.93 $mW/m\ K^2$ at 775 K.

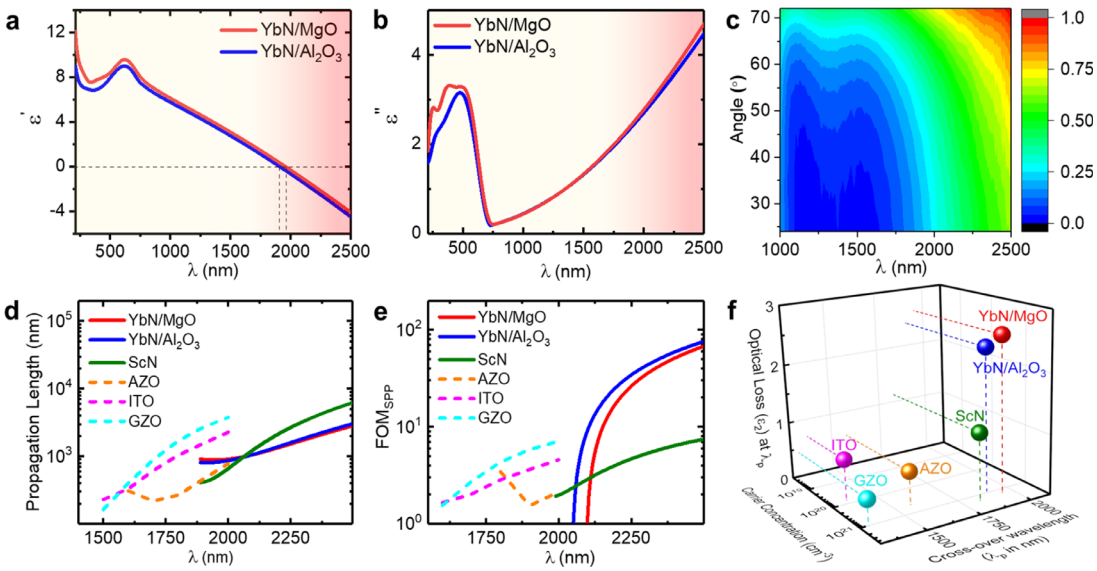

FIG. 5. (a) Real and (b) imaginary part of the dielectric function of YbN on MgO and Al_2O_3 substrates. (c) Angle-dependent reflection of YbN/MgO. Comparison of (d) propagation length (L), (e) figure-of-merit (FOM) of surface plasmon polariton (SPP), and (f) carrier concentration, crossover wavelength, and optical loss at crossover wavelength of YbN on both substrates with AZO, ITO, and GZO.

an alternative plasmonic material for infrared optics. In the 500–600 nm spectral range, because direct bandgap optical transition ε'' shows a peak while ε' exhibits a wiggle pattern because of the Krammer–Kronig relationship. The maximum ε' of 9.54 at 628 nm is consistent with its bandgap of ~2 eV and is comparable to the maximum ε' of ErN and ScN.[41,42] Angle-dependent reflection measurement of YbN/MgO in Fig. 5(c) shows a clear dip at 1300 nm due to typical *p-d* inter-band transitions[22] and another dip at plasma wavelength 1950 nm, further verifying the IR plasmonic response in YbN films.

A comparison of the important plasmonic properties of YbN thin films on two different substrates with other IR plasmonic materials like ScN, AZO, ITO, and GZO[41,43] is presented in Figs. 5(d) and 5(e). In the region beyond the crossover where YbN behaves like a metal, the surface-plasmon-polariton (SPP) propagation length (L) at the YbN-air interface and figure-of-merit (FOM) for SPP (FOM_{SPP}) is calculated from the experimental dielectric permittivity.[44,45] The propagation length is quite similar, and the FOM_{SPP} is much higher in YbN compared to other infrared IR plasmonic materials. However, Fig. 5(f) shows that optical loss (ε'') value is relatively higher for YbN compared to other IR plasmonic materials, essentially due to lower carrier mobility. Since the carrier mobility depends on the crystallinity of films, it could be increased to reduce the optical loss by altering the deposition conditions or with more advanced deposition techniques, such as molecular beam epitaxy. Therefore, these results suggest that YbN is a promising plasmonic material for short-wavelength infrared spectral range applications. A comparison of various other optical parameters, namely, optical loss, SPP decay length, relaxation time, figure-of-merit for localized SPP resonance, confinement width, and quality factor, is entailed in the supplementary material (see Fig. S5).

In conclusion, a high thermoelectric power factor of 1.93 mW/m K^2 at 750 K and high-quality short-wavelength infrared plasmonic response are reported in epitaxial rare-earth semiconducting YbN thin films deposited on (001) MgO substrates. Due to their epitaxial growth and good crystallinity, YbN thin films reported herein exhibit a record high mobility of 23.1 cm^2/V s at room temperature. The coexistence of high thermoelectric power factor and plasmonic response in YbN signifies that it could be a promising material for application in resonant thermoelectric nano-photonics. Consequently, they can be utilized for diverse applications, such as telecommunications, security, and sensing devices.

See the supplementary material for the details on sample preparation, HRXRD and FESEM characterization, XPS measurement, and optical, electrical, and thermoelectric characterization.

M.L. and B.S. acknowledge International Centre for Materials Science (ICMS) and Sheikh Saqr Laboratory (SSL) in JNCASR for support. B.S. acknowledges the Young Scientist Research Award (YSRA) from the Board of Research in Nuclear Sciences (BRNS), Department of Atomic Energy (DAE), India, with Grant No. 59/20/10/2020-BRNS/59020 for financial support. M.L. thanks the Council of Scientific & Industrial Research (CSIR) for a fellowship.

AUTHOR DECLARATIONS

Conflict of Interest

The authors have no conflicts to disclose.

Author Contributions

Mehak Loyal: Conceptualization (supporting); Data curation (lead); Formal analysis (lead); Writing – original draft (lead). **Bidesh Biswas:** Data curation (supporting); Formal analysis (supporting); Validation (supporting); Writing – original draft (supporting). **Prasanna Das:**

Data curation (supporting); Formal analysis (supporting); Writing – original draft (supporting). **Bivas Saha:** Conceptualization (lead); Formal analysis (equal); Funding acquisition (lead); Project administration (lead); Writing – review & editing (lead).

DATA AVAILABILITY

The data that support the findings of this study are available from the corresponding author upon reasonable request.

REFERENCES

[1] T. Yanagida, Opt. Mater. **35**(11), 1987–1992 (2013).
[2] T. Nakano, S. Masuyama, Y. Hirayama, T. Izawa, T. Nakagawa, Y. Fujimoto, T. Irie, E. Nakamura, and T. A. Yamamoto, Appl. Phys. Lett. **101**(25), 251908 (2012).
[3] K. P. O'Donnell and B. Hourahine, Eur. Phys. J. Appl. Phys. **36**(2), 91–103 (2006).
[4] D. Barbier, M. Rattay, F. Saint André, G. Clauss, M. Trouillon, A. Kevorkian, J. M. P. Delavaux, and E. Murphy, IEEE Photonics Technol. Lett. **9**(3), 315–317 (1997).
[5] B. Zheng, J. Yang, F. Qi, J. Wang, X. Zhang, and P. Wang, J. Non. Cryst. Solids **573**, 121129 (2021).
[6] J. Glodo, Y. Wang, R. Shawgo, C. Brecher, R. H. Hawrami, J. Tower, and K. S. Shah, Phys. Procedia **90**, 285–290 (2017).
[7] F. Natali, B. J. Ruck, N. O. V. Plank, H. J. Trodahl, S. Granville, C. Meyer, and W. R. L. Lambrecht, Prog. Mater. Sci. **58**(8), 1316–1360 (2013).
[8] N. O. V. Plank, F. Natali, J. Galipaud, J. H. Richter, M. Simpson, H. J. Trodahl, and B. J. Ruck, Appl. Phys. Lett. **98**(11), 112503 (2011).
[9] K. Senapati, M. G. Blamire, and Z. H. Barber, Nat. Mater. **10**(11), 849–852 (2011).
[10] P. Wachter, *Advances in Materials Physics and Chemistry* (Scientific Research Publishing, 2015), p. 96.
[11] J. K. Hite and J. M. Zavada, ECS J. Solid State Sci. Technol. **8**(9), P527 (2019).
[12] A. Gupta, R. Zhang, P. Kumar, V. Kumar, and A. Kumar, Magnetochemistry **6**(1), 15 (2020).
[13] S. Dong, J. K. Furdyna, and X. Liu, *Rare Earth and Transition Metal Doping of Semiconductor Materials* (Woodhead Publishing, 2016), pp. 129–167.
[14] T. Nakamura, V. R. Badarla, K. Hashimoto, P. G. Schunemann, and T. Ideguchi, Opt. Lett. **47**(7), 1790–1793 (2022).
[15] H. Huang, R. Li, S. Jin, Z. Li, P. Huang, J. Hong, S. Du, W. Zheng, X. Chen, and D. Chen, ACS Appl. Mater. Interfaces **13**(29), 34561–34571 (2021).
[16] A. R. Zanatta, J. Phys. D **42**(2), 025109 (2009).
[17] K. Upadhya, V. Bhatia, A. I. Kamalasanan Pillai, M. Garbrecht, and B. Saha, Appl. Phys. Lett. **118**(13), 132103 (2021).
[18] M. J. Hoffmann and G. Petzow, MRS Online Proc. Libr. **287**, 3 (1992).
[19] J. Jia and T. Yanagitani, Phys. Rev. Appl. **16**(4), 044009 (2021).
[20] R. Didchenko and F. P. Gortsema, J. Phys. Chem. Solids **24**(7), 863–870 (1963).
[21] H. R. Ott, H. Rudigier, and F. Hulliger, Solid State Commun. **55**(2), 113–116 (1985).
[22] L. Degiorgi, W. Bacsa, and P. Wachter, Phys. Rev. B **42**(1), 530 (1990).
[23] H. Warring, B. J. Ruck, J. F. McNulty, E. M. Anton, S. Granville, A. Koo, B. Cowie, and H. J. Trodahl, Phys. Rev. B **90**(24), 245206 (2014).
[24] P. Larson, W. R. L. Lambrecht, A. Chantis, and M. Van Schilfgaarde, Phys. Rev. B **75**(4), 045114 (2007).
[25] A. Murugan, R. Rajeswarapalanichamy, M. Santhosh, and K. Iyakutti, J. Magn. Magn. Mater. **385**, 441–450 (2015).
[26] F. Wu and W. Wang, J. Electron. Mater. **52**, 276–283 (2023).
[27] P. S. Thorup, C. M. Zeuthen, K. A. Borup, and B. B. Iversen, Chem. Mater. **34**(11), 5206–5214 (2022).
[28] D. Rao, O. Chowdhury, A. I. K. Pillai, G. K. Pradhan, S. Sahoo, J. P. Feser, M. Garbrecht, and B. Saha, ACS Appl. Energy Mater. **5**(6), 6847–6854 (2022).
[29] D. Rao, B. Biswas, E. Flores, A. Chatterjee, M. Garbrecht, Y. R. Koh, V. Bhatia, A. I. K. Pillai, P. E. Hopkins, M. Martin-Gonzalez, and B. Saha, Appl. Phys. Lett. **116**(15), 152103 (2020).
[30] Y. Ohno, J. Electron Spectrosc. Related Phenom. **165**(1–3), 1–4 (2008).
[31] S. Schmidt, S. Hüfner, F. Reinert, and W. Assmus, Phys. Rev. B. **71**(19), 195110 (2005).
[32] Y. Sohn, Ceram. Int. **44**(3), 3341–3347 (2018).
[33] K. Upadhya, R. Kumar, Q. Li, B. Sun, and B. Saha, Phys. Rapid Res. Lett. **16**(6), 2200029 (2022).
[34] K. C. Maurya, B. Biswas, M. Garbrecht, and B. Saha, Phys. Status Solidi RRL **13**(9), 1900196 (2019).
[35] B. Biswas, S. Chakraborty, O. Chowdhury, D. Rao, A. I. K. Pillai, V. Bhatia, M. Garbrecht, J. P. Feser, and B. Saha, Phys. Rev. Mater. **5**(11), 114605 (2021).
[36] B. Saha, M. Garbrecht, J. A. Perez-Taborda, M. H. Fawey, Y. R. Koh, A. Shakouri, M. Martin-Gonzalez, L. Hultman, and T. D. Sands, Appl. Phys. Lett. **110**, 252104 (2017).
[37] W. Orellana and H. Chacham, Phys. Rev. B **62**, 10135 (2000).
[38] S. R. Popuri, M. Pollet, R. Decourt, F. D. Morrison, N. S. Bennett, and J. W. G. Bos, J. Mater. Chem. C **4**(8), 1685–1691 (2016).
[39] L. Gao, J. Zhu, H. Wang, F. Ren, and B. Zhao, J. Phys. D **45**(18), 185303 (2012).
[40] H. Takiguchi, A. Matoba, K. Sasaki, Y. Okamoto, H. Miyazaki, and J. Morimoto, Mater. Trans. **51**(5), 878–881 (2010).
[41] K. C. Maurya, D. Rao, S. Acharya, P. Rao, A. I. K. Pillai, S. K. Selvaraja, M. Garbrecht, and B. Saha, Nano Lett. **22**(13), 5182–5190 (2022).
[42] P. Das, K. C. Maurya, J. L. Schroeder, M. Garbrecht, and B. Saha, ACS Appl. Energy Mater. **5**(4), 3898–3904 (2022).
[43] G. V. Naik, V. M. Shalaev, and A. Boltasseva, Adv. Mater. **25**(24), 3264–3294 (2013).
[44] K. C. Maurya, V. M. Shalaev, A. Boltasseva, and B. Saha, Opt. Mater. Express **10**(10), 2679 (2020).
[45] P. Das, B. Biswas, K. C. Maurya, M. Garbrecht, and B. Saha, ACS Appl. Mater. Interfaces **14**(41), 46708–46715 (2022).